Eur. Phys. J. A **22**, 277–291 (2004)
DOI 10.1140/epja/i2004-10033-9

THE EUROPEAN PHYSICAL JOURNAL A

Photoproduction of π^0-mesons from nuclei

B. Krusche[1,a], J. Lehr[2], J. Ahrens[3], J.R.M. Annand[4], R. Beck[3], F. Bloch[1], L.S. Fog[4], D. Hornidge[3], S. Janssen[5], M. Kotulla[1], J.C. McGeorge[4], I.J.D. MacGregor[4], J. Messchendorp[5], V. Metag[5], U. Mosel[2], R. Novotny[5], R.O. Owens[4], M. Pfeiffer[5], R. Sanderson[4], S. Schadmand[5], and D.P. Watts[4]

[1] Department of Physics and Astronomy, University of Basel, CH-4056 Basel, Switzerland
[2] Institut für Theoretische Physik I, Universität Giessen, D-35392 Giessen, Germany
[3] Institut für Kernphysik, Johannes-Gutenberg-Universität Mainz, D-55099 Mainz, Germany
[4] Department of Physics and Astronomy, University of Glasgow, Glasgow G12 8QQ, UK
[5] II. Physikalisches Institut, Universität Giessen, D-35392 Giessen, Germany

Received: 2 February 2004 /
Published online: 3 November 2004 –
Communicated by R. Milner

Abstract. Photoproduction of neutral pions from nuclei (carbon, calcium, niobium, lead) has been studied for incident-photon energies from 200 MeV to 800 MeV with the TAPS detector using the Glasgow photon tagging spectrometer at the Mainz MAMI accelerator. Data were obtained for the inclusive photoproduction of neutral pions and the partial channels of quasifree single-π^0, double-π^0, and $\pi^0\pi^\pm$ photoproduction. They have been analyzed in terms of the in-medium behavior of nucleon resonances and the pion-nucleus interaction. They are compared to earlier measurements from the deuteron and to the predictions of a Boltzmann-Uehling-Uhlenbeck (BUU) transport model for photon-induced pion production from nuclei.

PACS. 13.60.Le Meson production – 25.20.Lj Photoproduction reactions

1 Introduction

The study of meson photoproduction from nuclei is motivated by two strongly interrelated aspects, namely possible in-medium modifications of hadrons and the meson-nucleus interaction. The in-medium properties of mesons and nucleon resonances is a topic which is hotly debated. However, with the exception of the Δ-isobar, experimental results are still scarce and partly contradictory. In-medium modifications of nucleon resonances may arise from many different effects. The most trivial one is the broadening of the excitation functions due to Fermi motion of the bound nucleons. Pauli blocking of final states decreases the decay widths but this is counterbalanced by collisional broadening due to resonance-nucleon scattering. In particular, for the $D_{13}(1520)$ it has been found in [1–3] that a large collisional broadening can be generated from π and ρ exchange and that the in-medium width is sensitive to modifications of the spectral functions of these mesons. Besides such conventional effects arising from meson-nucleon scattering, additional mechanisms [4,5] could lead to a shift of spectral strength of the ρ-meson to smaller invariant masses, thus further enhancing the width of the D_{13}.

Photon-induced reactions are particularly well suited to study such effects since photons probe the entire nuclear volume. Reactions induced by strongly interacting particles like pions are always restricted to the surface region and thus probe a lower effective density. The first experimental investigation of the nuclear response in the resonance region to photons was done with total photoabsorption measurements [6,7] for nuclei ranging from ^{7}Li to ^{238}U. Total photoabsorption has the advantage that no final-state interaction (FSI) effects must be accounted for so that indeed the entire nuclear volume is probed. As a consequence, when scaled by the atomic mass number, the total cross-sections from all nuclei fall practically on the same curve ("universal curve"). This curve shows a clear signal for the Δ resonance but no evidence of the bumps observed for the free nucleon in the second and third resonance regions (see fig. 1). This result of the experiments was surprising and is even today not fully understood.

The situation is complicated by the already complex structure of the resonance peak for the free proton. The resonance consists of a superposition of reaction channels which differ in their energy dependence (see fig. 1). Most of the rise of the cross-section to the maximum around 700 MeV comes from double-pion production. The interpretation of double-pion photoproduction is complicated (see [8] for a recent overview), but it is known

[a] e-mail: Bernd.Krusche@unibas.ch

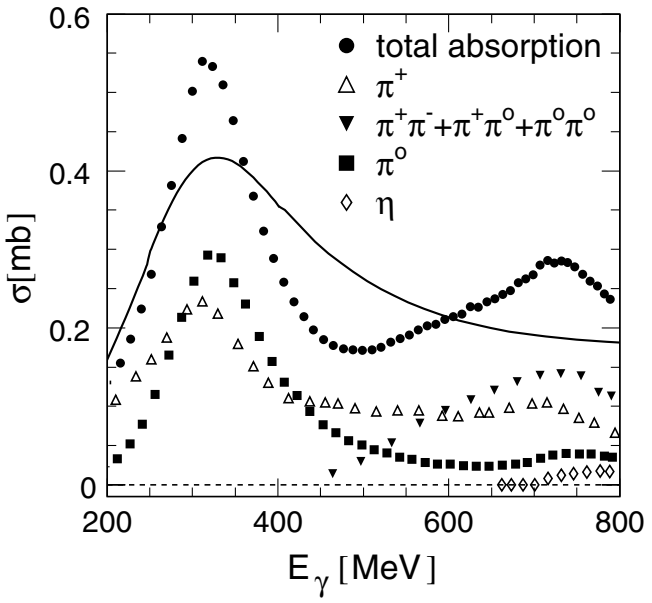

Fig. 1. Total photoabsorption on the proton and on nuclei. The symbols show the total cross-section and the decomposition into partial reaction channels for the proton [9–14]. Solid curve: average of the total photoabsorption cross-sections for nuclei scaled to their mass numbers [7].

that contributions, which are not related to the excitation of resonances in the second resonance region, are significant. In particular, Δ-Kroll-Rudermann and Δ pion-pole terms dominate the $\pi^+\pi^-$ final state which has the largest cross-section of all double-pion channels. Gomez Tejedor and Oset [15] have pointed out that for this channel the peaking of the cross-section around 700 MeV is related to an interference between the leading Δ-Kroll-Rudermann term and the sequential decay of the D_{13}-resonance via $D_{13} \rightarrow \Delta\pi$. Hirata *et al.* [16] have subsequently argued that the change of this interference effect in the nuclear medium is one of the most important reasons for the suppression of the bump structure.

Inclusive reactions like total photoabsorption alone do not allow a detailed investigation of such effects. A study of the partial reaction channels is desirable. The experimental identification of exclusive final states is more involved and FSI effects must be accounted for. The interpretation of exclusive measurements therefore always needs models which account for the trivial in-medium and FSI effects like absorption of mesons and propagation of mesons and resonances through nuclear matter. On the other hand, as a by-product, the analysis of the FSI effects enables the study of meson-nucleus interactions.

During the last few years, in a series of experiments with the TAPS detector at MAMI in Mainz, we have studied exclusive photoproduction reactions from heavy nuclei which can be related to the excitation of certain resonances or production mechanisms. The most specific reaction in this respect is the photoproduction of η-mesons which proceeds in the second resonance region almost entirely through the excitation of the $S_{11}(1535)$-resonance [11,17]. In this case no unexplained depletion of the in-medium strength was found [18], which is in line with theoretical findings [3,19] that the change of the S_{11} self-energy in the medium is rather small. The data were in excellent agreement with model calculations that take the trivial in-medium effects and FSI into account [20, 21]. A similar result was later found by Yorita *et al.* [22], who measured the η excitation function to somewhat higher incident-photon energies. In a recent study [23], it was shown that the data could be described over the full energy range by applying a momentum-dependent S_{11} nuclear potential. An attempt to study the in-medium properties of the D_{13}-resonance was undertaken with a measurement of quasifree single-π^0 photoproduction [24]. Again in contrast to total photoabsorption the second resonance bump was clearly visible. On the free nucleon, the structure in this reaction is almost entirely due to the D_{13}-resonance. A comparison to deuteron data showed no broadening in nuclei and provided no evidence for an increased in-medium width of the D_{13}. On the other hand, theoretical models [3,2] predict such a modification. However, as discussed below, exclusive reaction channels are dominated by the nuclear surface region where in-medium effects are smaller. This is mostly due to FSI effects. Furthermore, as discussed in [25], even in the absence of FSI, resonance broadening effects are suppressed in reactions which do not contribute to the broadening. The reason is that when the total width Γ of a resonance increases as a function of the nuclear density ρ (*e.g.*, due to collisional broadening), the branching ratio $b_f = \Gamma_f/\Gamma$ for any other decay channel f, which does not contribute to the broadening, decreases as function of density. Due to this effect, contributions from the broadened resonance to such exclusive final states are suppressed in the average over the nuclear volume.

In the present paper we collect the results for all reaction channels which involve π^0 photoproduction from nuclei. Data have been obtained for the inclusive reaction, where inclusive means that all final states with at least one π^0-meson were accepted. Furthermore, the quasifree contributions of single-π^0, double-π^0, and $\pi^0\pi^\pm$ photoproduction have been determined. The data are compared to the results of a semi-classical Boltzmann-Uehling-Uhlenbeck (BUU) transport model [26,27] which accounts for medium effects such as Fermi motion, nuclear binding, Pauli blocking, resonance broadening and includes a realistic description of the FSI. The treatment follows the trajectories of the particles through the nucleus and therefore yields additional information not accessible to experiment.

2 Experimental setup

The experiments were carried out at the Glasgow tagged photon facility [28] installed at the Mainz MAMI accelerator [29]. The tagged photon facility uses bremsstrahlung photons produced with the 855 MeV electron beam in a radiator foil. The scattered electrons are detected in the focal plane of the tagging spectrometer with an energy resolution of $\approx$ 2 MeV. The experiments covered

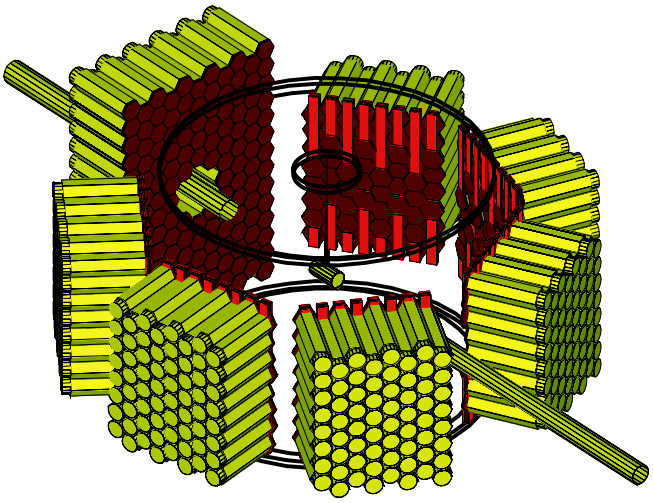

Fig. 2. Setup of the TAPS detector at the Mainz MAMI accelerator. The beam entered the target chamber from the lower right edge.

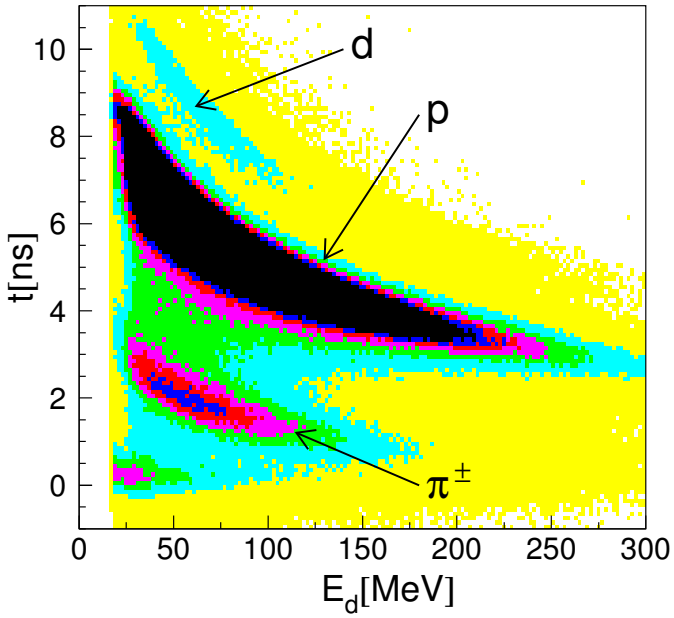

Fig. 3. Time-of-flight *versus* the energy deposited in the BaF_2 detectors. Three bands corresponding to deuterons, protons, and charged pions are visible (photons already eliminated).

the photon energy range 200–800 MeV. Solid targets with thicknesses of 25 mm (C), 10 mm (Ca), 2.1 mm (Nb), and 0.47 mm (Pb), corresponding to roughly 0.1 radiation lengths were irradiated. The diameter of the targets was 50 mm and the beam spot size at target position was approximately 30 mm. The neutral pions were detected, via their two-photon decays, with the electromagnetic calorimeter TAPS [30,31]. The individual modules of the calorimeter are hexagonally shaped BaF_2 crystals of 25 cm length with an inner diameter of 5.9 cm. The inclusive and single-π^0 photoproduction data were obtained with the setup discussed in [14]. The BaF_2 modules were arranged in 5 blocks, each containing 8×8 modules. With the exception of the backward block, all modules were equipped with individual plastic veto detectors. The blocks were placed in one plane around the target at a distance of 55 cm at polar angles of $\pm 38°$, $\pm 88°$, and $+133°$. The double-pion production reactions were studied with an upgraded version of the TAPS detector covering a larger solid angle (see fig. 2). In this setup 6 blocks with 64 modules and a forward wall with 138 BaF_2 modules were used. The blocks were placed 55 cm away from the targets at polar angles of $\pm 54°$, $\pm 103°$, and $\pm 153°$, while the forward wall was placed 60 cm away from the target center.

3 Data analysis

The discrimination between photons and particles was done with the aid of the plastic veto detectors, a time-of-flight analysis, and a pulse shape analysis of the signals from the BaF_2 scintillators in the same way as discussed in [14]. Neutral pions were identified with a standard invariant mass analysis of photon pairs. In addition to the analysis in [14], charged pions for the extraction of the $\pi^0\pi^\pm$ cross-section were identified from time-of-flight *versus* energy plots. A typical example for this analysis is shown in fig. 3. Photons have already been eliminated by the methods mentioned above and only charged hits, with an identified π^0-meson in coincidence, are included. Background from random coincidences between TAPS and the tagging spectrometer was determined by shifting the time-of-flight cut away from the prompt peak. The absolute normalization of the cross-sections was done as described in detail in [14] for the measurement with the deuterium target.

3.1 Inclusive π^0 photoproduction

All events with at least one π^0 identified via the invariant-mass analysis were accepted without any further kinematic cuts. Combinatorial background from pairs of photons originating from the decay of different pions was fitted and subtracted in the invariant-mass spectra (see ref. [14] for typical invariant-mass spectra). For differential cross-sections this was done separately for each bin of the respective observable.

The energy- and angle-dependent detection efficiency of the TAPS detector was determined with Monte Carlo simulations, carried out with the GEANT3 code [32]. It was previously shown that such simulations reproduce the photon response of TAPS precisely [31]. Inclusive π^0 production is a complicated mixture of different reaction channels. With the exception of coherent single-π^0 production all channels have at least a three-body final state and all are subject to final-state interaction processes. Consequently, no reliable models exist which could be used as event generators for the Monte Carlo simulations. However, the detection efficiency $\epsilon(\Theta_{\pi^0}, T_{\pi^0})$ can only depend on the laboratory polar angle Θ_{π^0} and the laboratory kinetic energy T_{π^0} of the pions (the dependence on the

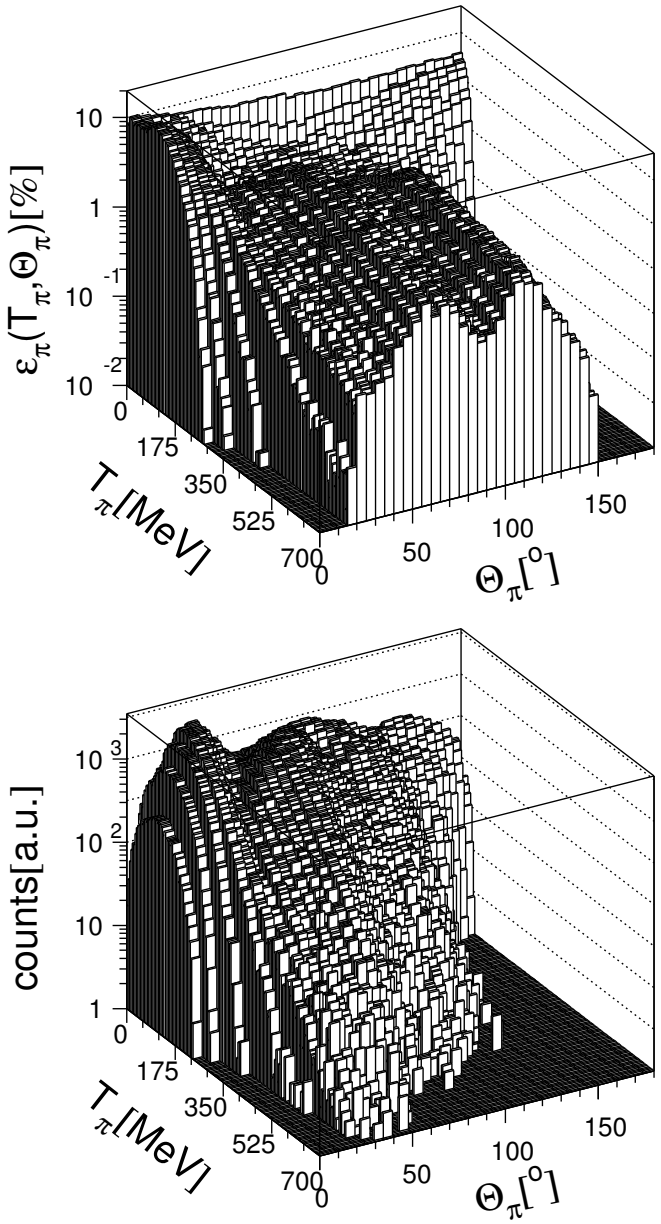

Fig. 4. Detector acceptance for π^0-mesons as a function of the laboratory polar angle and the laboratory kinetic energy of the mesons. Upper part: efficiency calculated with a Monte Carlo simulation. Lower part: measured distribution of pions, not corrected for acceptance, for incident-photon energies from 200–800 MeV.

azimuthal angle Φ can be easily integrated out since no polarization degrees of freedom are involved). Since Θ_{π^0} and T_{π^0} are measured, the efficiency can be corrected individually for each detected π^0-meson. This method generates a model-independent result for the cross-section as long as the efficiency does not vanish for any kinematically possible combination of Θ_{π^0} and T_{π^0}. The simulated efficiency is plotted in the upper part of fig. 4. The plot demonstrates that although the overall efficiency is not high, there is only a small region in the (Θ_{π^0},T_{π^0})-plane at kinetic energies larger than 200 MeV and forward angles smaller than 15° where no π^0-mesons can be detected. This is so, since in the energy range of interest almost always some fraction of the decay photon pairs of π^0-mesons falls within the spectrometer acceptance. Kinetic energies larger than 700 MeV are impossible for incident-photon energies $\leq$ 800 MeV and the zero-efficiency region at backward angles also corresponds to a kinematically forbidden region. As an example of a measured distribution, the bottom part of fig. 4 shows the data for ^{40}Ca. The small acceptance gap at forward angles was corrected with a phase space simulation. This is not model independent, but the largest corrections to the total cross-sections are below 5% so that possible systematic uncertainties arising from the acceptance gap are certainly below the 1% level.

The inclusive cross-section $\sigma_{\rm incl}$ determined this way can be written in the following form:

$$\sigma_{\rm incl} = \sigma_{\pi^0} + 2\sigma_{2\pi^0} + \sigma_{\pi^0\pi^+} + \sigma_{\pi^0\pi^-} + \beta\sigma_\eta \ , \qquad (1)$$
$$\beta = 3b_{\eta\to 3\pi^0} + b_{\eta\to\pi^0\pi^+\pi^-} \approx 1.2 \ ,$$

where σ_x are the partial cross-sections labeled with the different final states and b_i are the branching ratios of the η-meson for the respective decay channels. It was previously shown in [14] that this relation holds very accurately in case of the deuteron, where all partial cross-sections are known. This means in particular that final states with pion multiplicity larger than two, which do not originate from decays of the η-meson, are negligible in this energy range. Provided the partial cross-sections for η and double-π^0 production are known, the part $\sigma_{\rm nm}$ of the total photoabsorption cross-section $\sigma_{\rm abs}$ with at least one neutral pion or one η-meson in the final state follows from

$$\sigma_{\rm nm} = \sigma_{\rm incl} - \sigma_{2\pi^0} - (\beta - 1)\sigma_\eta \ . \qquad (2)$$

The total photoabsorption cross-section $\sigma_{\rm abs}$ can then be split into

$$\sigma_{\rm abs} = \sigma_{\rm nm} + \sigma_{\rm cm} + \sigma_{\rm r} \ , \qquad (3)$$

where $\sigma_{\rm cm}$ corresponds to reactions which have no neutral meson but at least one charged pion in the final state, and $\sigma_{\rm r}$ corresponds to final states without any mesons. In case of the deuteron, $\sigma_{\rm r}$ equals the deuteron photo-breakup.

3.2 Exclusive reaction channels

The decomposition of the inclusive process into exclusive reaction channels is discussed in detail in [14] for the deuteron target, but it is less straightforward for heavy nuclei. The larger Fermi momenta cause a stronger smearing of kinematical observables, and FSI affects the reaction products. The first step is the separation of quasifree single-π^0 photoproduction. Since the solid-angle coverage of the detector amounts only to $\approx$ 25% of 4π this must be done with cuts on the reaction kinematics. Missing-energy (ΔE_π) spectra can be constructed for the kinetic energy $E^\star_\pi$ of the pion in the center-of-momentum (cm) frame of the incident photon and a stationary nucleon:

$$\Delta E_\pi = E^\star_\pi(\gamma_1\gamma_2) - E^\star_\pi(E_{\rm b}) \ . \qquad (4)$$

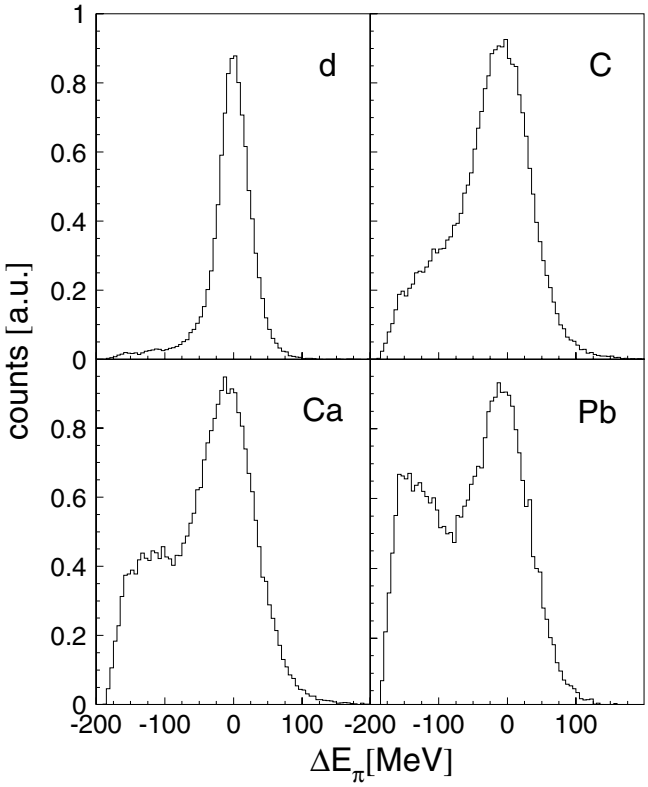

Fig. 5. Missing-energy spectra for π^0 photoproduction for incident-photon energies 395–440 MeV calculated under the assumption of quasifree kinematics.

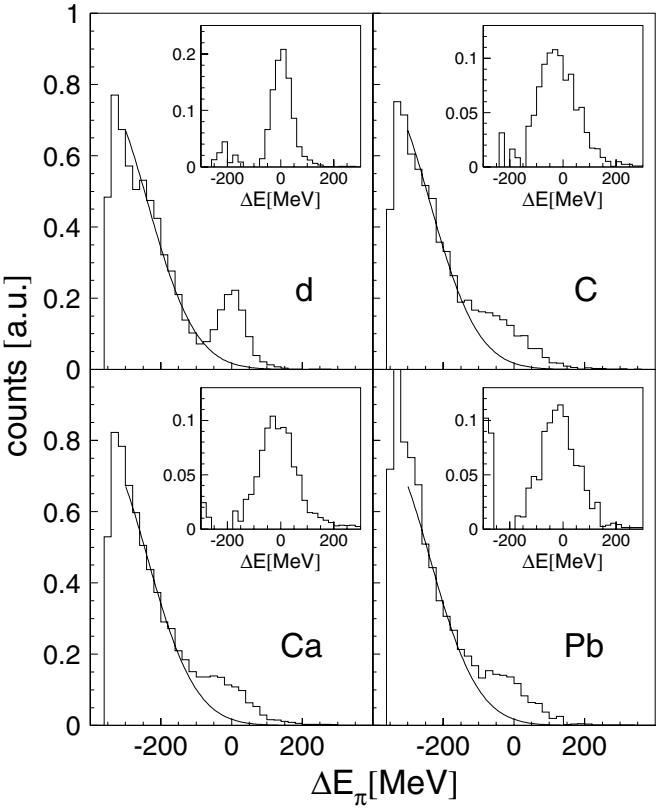

Fig. 6. Missing-energy spectra for π^0 photoproduction for incident-photon energies of 790 MeV calculated under the assumption of quasifree kinematics.

Here, $E^\star_\pi(E_\mathrm{b})$ is the pion energy derived from the energy of the incident-photon beam E_b and $E^\star_\pi(\gamma_1\gamma_2)$ is reconstructed from the momenta of the pion decay photons.

The reaction kinematic is assumed to be quasifree, *i.e.* the pion is produced from one participant nucleon and the rest of the nucleus acts as spectator. The neglect of the Fermi momenta of the bound nucleons simply broadens the missing-energy peaks. At low incident-photon energies a significant fraction of π^0 photoproduction stems from the coherent reaction, in which the recoil is not taken by a nucleon but by the whole nucleus. A previously published analysis [33] has separated the coherent parts with a missing-energy analysis assuming coherent kinematics which gives much narrower peaks since no Fermi smearing is involved. In the present analysis contributions from the coherent reaction fall within the broader peak of quasifree pion production.

An example of the missing-energy spectra at medium incident-photon energy around 420 MeV is shown in fig. 5. There is a striking difference between the missing-energy distribution from the deuteron and from heavy nuclei. At these energies, in case of the deuteron a peak with a small tail at negative values is visible. The tail is due to the onset of double-pion production which has, however, a relatively small cross-section in this energy region. On the other hand, the distribution for lead shows a substantial non-quasifree background. At this photon energy the background arises mainly from single-pion production with significant final-state interaction of the pion or from two-body contributions to the production process. It must be emphasized that the single-π^0 production cross-section $\sigma^{\mathrm{qf}}_{\pi^0}$ obtained from this kinematical analysis is not identical with the cross-section σ_{π^0} in eq. (1). By definition σ_{π^0} is the cross-section for events with one and only one neutral pion in the final state, it does not matter if the quasifree-energy relation is valid. However, single-π^0 events, in which the π^0 suffers an FSI or was produced by a two-body interaction, will in general be excluded from $\sigma^{\mathrm{qf}}_{\pi^0}$. Only for the deuteron, where FSI and two-body absorption do not significantly contribute, we have $\sigma^{\mathrm{qf}}_{\pi^0} \approx \sigma_{\pi^0}$. At higher incident-photon energies, much larger contributions from multiple-pion final states are visible in the missing-energy distributions. An example is shown in fig. 6. This figure shows also the lineshape of the missing-energy peaks, which are broader for the heavy nuclei due to Fermi motion. The shape of the background (solid curves in fig. 6) was fitted to the deuteron data and then scaled for the nuclei. The similarity of the background shapes for the deuteron and the heavy nuclei is not surprising. The background for the deuteron and the nuclei is dominated by the same source, namely double-pion events where only one pion was detected. Folding the curve with a typical momentum distribution for nucleons bound in heavy nuclei has not much effect since already the slope for the deuteron is not steep. However, fitting and subtracting

the background contributions would introduce systematic uncertainties which are difficult to control for the comparison to model predictions. We have therefore extracted the quasifree single-π^0 production with a cut in the missing-energy spectra from 0–200 MeV, assuming symmetric lineshapes. Contributions from the tail of the background distribution were assumed to be negligible as suggested by fig. 6. The same analysis was applied to the results of the BUU calculations so that systematic effects in the comparison between data and model results are minimized.

The analysis of double-π^0 photoproduction from the proton and the deuteron is discussed in detail in [14,13, 34,35]. At incident-photon energies below the η production threshold the cross-sections of all other reactions with at least three photons in the final state are negligible compared to double-π^0 production. Therefore, an analysis of all events with at least three identified photons is sufficient for the double-π^0 channel. Background may only arise from particles which are misidentified as photons or from false photon pairs which result from the split-off of an electromagnetic shower into two geometrically unrelated components. Particles were completely suppressed with the veto detectors, the pulse shape analysis and the time-of-flight analysis. Subsequently, a standard invariant-mass analysis was used to assign two photons (labeled γ_1, γ_2) to the decay of one π^0. The third photon (γ_3) was then a candidate for a second π^0 decay with one undetected photon. Among the latter, split-off photons were suppressed with cuts on the relative timing ($\Delta t_{\gamma\gamma} \leq$1 ns for all photon combinations), the minimum energy of the third photon ($E_{\gamma_3} \geq$45 MeV), and the minimum opening angle between the third photon and the other two photons ($\Theta_{\gamma_1\gamma_3}$, $\Theta_{\gamma_2\gamma_3} \geq 20°$).

The above analysis was only used for the data measured with the first setup where the small solid-angle coverage resulted in a very low detection efficiency for events with four photons. A much more restrictive analysis is used for events with four detected photons which can be combined into two pairs with the invariant mass of the pion. A two-dimensional representation of the invariant masses of the photon pairs is shown in fig. 7. All possible combinations of the four photons into two pions are tested and the "best" combination is chosen via a χ^2 analysis. Only these "best" combinations are shown in the figure. After a cut on the invariant-mass peak a missing-mass analysis as discussed in [14] serves as a kinematical constraint. The mass of the missing particle (the participant nucleon) is calculated from the momenta $\mathbf{P}_{\gamma_i}$ and the energies E_{γ_i} of the pion decay photons and the beam energy E_b and compared to the nucleon mass m_N. Fermi motion is again neglected. The missing mass ΔM is given by

$$\Delta M = \sqrt{\left(E_\mathrm{b} + m_N - \sum_{i=1}^{4} E_{\gamma_i}\right)^2 - \left(\mathbf{P}_\mathrm{b} - \sum_{i=1}^{4} \mathbf{P}_{\gamma_i}\right)^2} - m_N. \quad (5)$$

Missing-mass spectra for calcium below and above the η production threshold are shown in fig. 8. At incident-photon energies below the η production threshold only a broad peak around zero is visible which agrees with

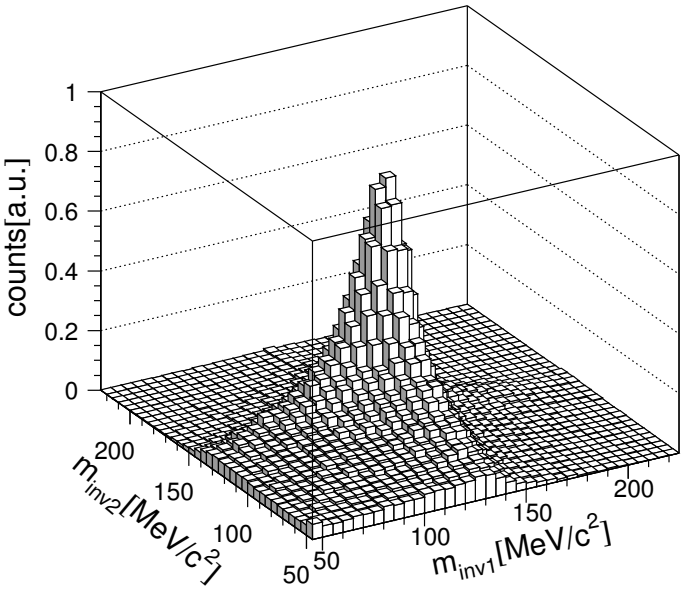

Fig. 7. Invariant mass of photon pair 1 *versus* invariant mass of photon pair 2 for events with four detected photons.

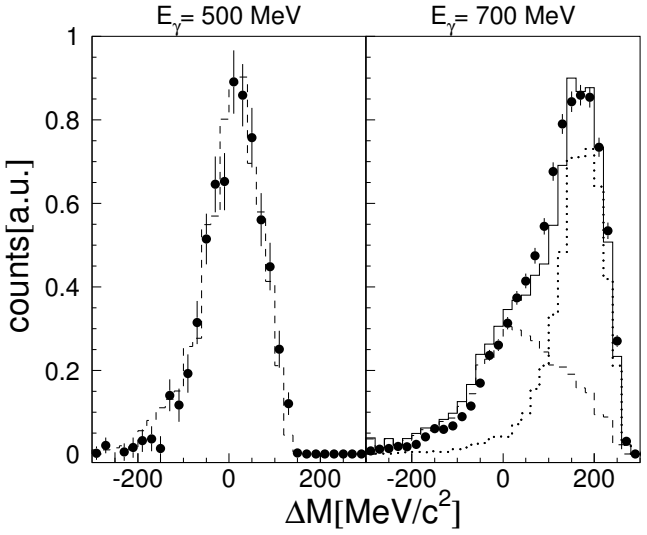

Fig. 8. Missing-mass spectra for double-π^0 photoproduction from Ca. Left side: incident-photon energy of 500 MeV (below η threshold), Right side: incident-photon energy 700 MeV (above η threshold). Closed circles: experiment, dashed histograms simulation of $2\pi^0$ photoproduction, dotted histogram: simulated contribution of η photoproduction, solid histogram: sum of both.

the result of a Monte Carlo simulation taking into account Fermi motion, a simple approximation for the final-state interaction, and the instrumental acceptance and detection efficiency. At higher incident-photon energies background from the $\eta \to 3\pi^0$ decay appears. In contrast to the deuteron case [14,34], the broadening of the peak due to Fermi motion and FSI is so large that no clear separation from the η background is possible. However, since the cross-section for η photoproduction from nuclei is known from the analysis of the 2γ decay channel of the η-meson

it can be subtracted. Simulations of double-π^0 production and the η background are compared to the data in fig. 8. The shape of the sum of the two contributions again agrees with the data.

An analogous analysis was done for the $\pi^0\pi^\pm$ reaction. The relative contribution of the η background is much smaller in this case. For the free nucleon $\sigma(\gamma N \to \pi^0\pi^\pm)$ is almost six times larger than $\sigma(\gamma N \to \pi^0\pi^0)$, while the branching ratio for $\eta \to \pi^+\pi^-\pi^0$ is a factor of 1.4 smaller than for $\eta \to 3\pi^0$.

The detection efficiency for double-π^0 events cannot be constructed in the model-independent way used for inclusive and single-π^0 photoproduction since the angles and energies of the pions are correlated. The case of $\pi^0\pi^\pm$ photoproduction is even more difficult since certain regions of the polar angle of the charged pions are not within the acceptance of the detector (spaces between blocks). Therefore, a phase space simulation of the reactions, including the effects of Fermi motion and a simple approximation of meson final-state interaction was used. For the latter only re-scattering of the pions was considered and the strength of this FSI was varied until all angular, energy and missing-mass distributions of the input to the simulations where consistent with the data (see, *e.g.*, fig. 8). From the comparison of different simulations and the good agreement between the analysis of the three-photon events from the first measurement and the four-photon events from the second measurement of double-π^0 production (see fig. 20) we estimate a systematic uncertainty of 5%.

4 The BUU model

In this section we discuss the main ingredients of the BUU transport model. For the present calculations we use the version discussed in detail in [26,27].

The model is based on the BUU equation which describes the space-time evolution ($\mathbf{r}$: space coordinate, $\mathbf{p}$: momentum) of the spectral phase space density F_i of an ensemble of interacting particles of type $i = N$, $P_{33}(1232)$, π, η, ... with mass μ:

$$\left(\frac{\partial}{\partial t} + \boldsymbol{\nabla}_p H \cdot \boldsymbol{\nabla}_r - \boldsymbol{\nabla}_r H \cdot \boldsymbol{\nabla}_p\right) F_i(\mathbf{r}, \mathbf{p}, \mu; t) = I_{\mathrm{coll}}[F_N, F_\pi, F_{P_{33}(1232)}, F_\eta, \ldots] \,. \quad (6)$$

The left-hand side —the Vlasov term— describes the propagation of the particles under the influence of a Hamilton function H, given by the expression

$$H = \sqrt{(\mu + S)^2 + p^2}, \quad (7)$$

which in the case of baryons contains an effective scalar potential S [27]. The right-hand side of the BUU equation (called the collision integral) consists of a gain and a loss term for the phase space density F_i at the different space-time points, accounting for interactions between the particles beyond the mean-field potential. The collision integral contains collision rates for the different reaction types such as baryon-baryon and baryon-meson collisions, resonance formation and decay. They include cross-sections for these processes and Pauli-blocking factors for outgoing fermions. Due to the reactions of different particle types we end up with a set of coupled BUU equations, which is solved by a test particle ansatz. This converts the continuous phase space density into an ensemble of discrete test particles propagating according to Hamilton's equations of motion.

Before the actual reaction, the nucleon test particles are initialized in the nucleus according to a Woods-Saxon density function in coordinate space. In momentum space, we make use of the local density approximation, distributing the nucleons homogeneously in the Fermi sphere corresponding to the local density. For the baryons, the mean-field potential S is determined as described in [27]. In this work, we focus on a momentum-dependent potential corresponding to an equation of state with medium compressibility.

The photon-nucleus reaction is modeled in terms of the absorption of the photon on a single nucleon, leading to final states $P_{33}(1232)$, $D_{13}(1520)$, $S_{11}(1535)$, $F_{15}(1680)$, $N\pi$, $N\pi\pi$, NV (V=ρ, ω, ϕ), $K\Lambda$, $K\Sigma$ and $K\bar{K}N$. These entry states are selected with probabilities corresponding to the different reaction cross-sections. They are then subjected to the final-state interactions, which are described by the set of BUU equations. The cross-sections for the γA reaction are then determined by averaging over an ensemble of such elementary reactions as outlined in [20].

Besides Fermi motion, binding effects and Pauli blocking we also account for collisional broadening of the most important resonances $P_{33}(1232)$, $D_{13}(1535)$ and $S_{11}(1535)$. For the in-medium width of the P_{33}, we either use the results of Oset *et al.* [36] or the phenomenological spreading potential of Hirata *et al.* [37], both giving roughly $\Gamma_{\mathrm{coll}} = 80$ MeV at saturation density ρ_0. The latter is interpreted as fully absorptive, whereas the absorption part in [36] is only about 40 MeV at ρ_0. For the $D_{13}(1520)$ and the $S_{11}(1535)$, we make use of the results of the self-consistent resonance-hole model in [3]. In particular, for the D_{13} a total collision width of $200\rho/\rho_0$ MeV at density ρ is used, while the S_{11} collision width is rather small and amounts only to $30\rho/\rho_0$ MeV. In both cases, one quarter of the total width is used for the absorptive channels.

5 Results and discussion

5.1 Inclusive π^0 photoproduction

The total inclusive π^0 cross-section σ_{incl} for the heavy nuclei is compared in fig. 9 to the deuteron cross-section. The cross-sections are scaled by A_{eff} which throughout the paper is defined as $A_{\mathrm{eff}} = 2$ for the deuteron and $A_{\mathrm{eff}} = A^{2/3}$ for the other nuclei. In this way, the average nucleon cross-section is compared to the nuclear cross-sections scaled in proportion to the nuclear surfaces. The shape of the total cross-sections for the heavy nuclei is similar, but it differs from the deuteron. The peak in the Δ-resonance region is broader for the heavier nuclei

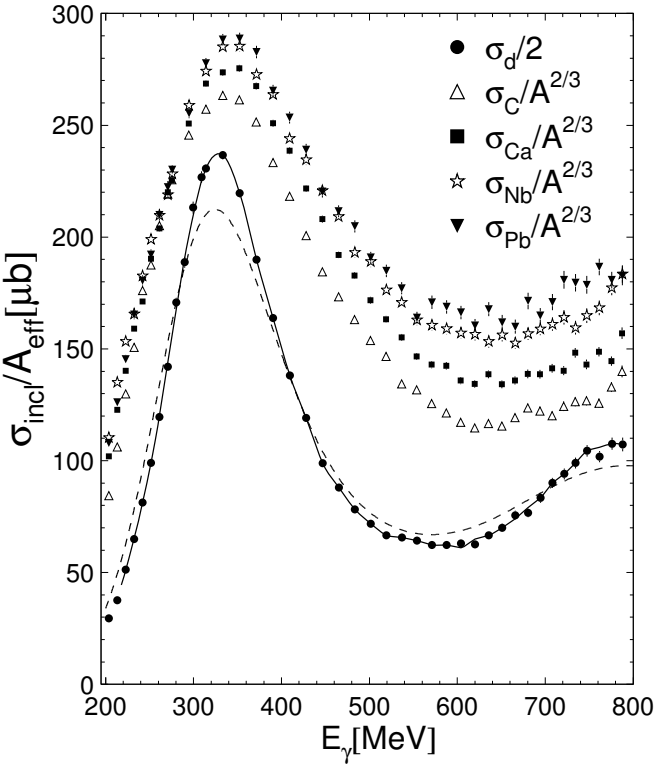

Fig. 9. Scaled total cross-section $\sigma_{\rm incl}$ of inclusive π^0 photoproduction from deuterium, carbon, calcium, niobium, and lead *versus* incident-photon energy (scale factor 1/2 for the deuteron, $A^{2/3}$ for all other nuclei). The solid line is only to guide the eye, the dashed line corresponds to the deuteron data folded with the momentum distribution of nucleons in calcium.

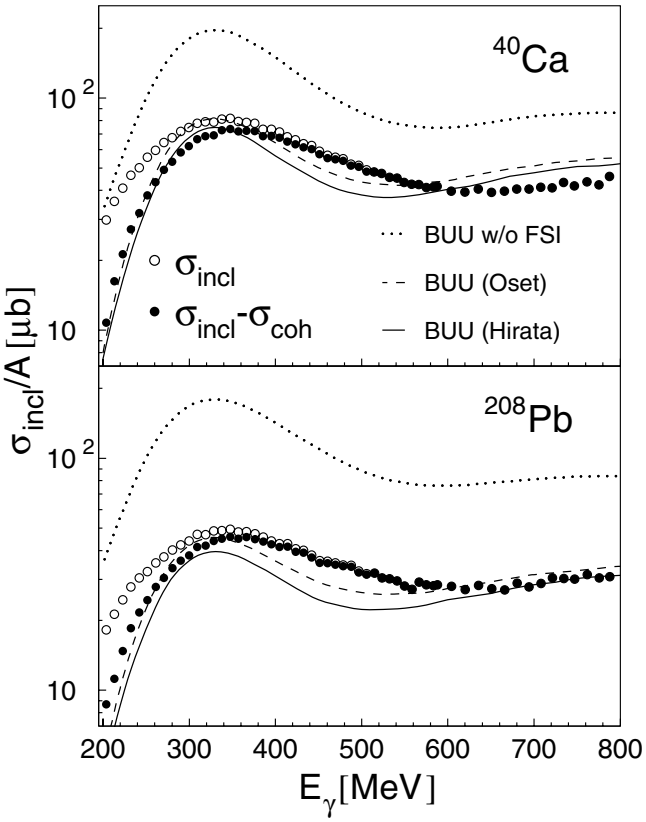

Fig. 10. Comparison of the inclusive cross-section $\sigma_{\rm incl}$ to BUU model calculations for calcium and lead. Open symbols: inclusive reaction, filled symbols: difference of inclusive and coherent reaction. Curves: BUU without FSI (dotted), BUU with FSI, Δ in-medium width from [36] (dashed) or [37] (solid).

and shifted to a higher energy. Furthermore, the valley between the first and second resonance region is much more pronounced for the deuteron. The different shape is not explained by the larger Fermi momenta of the nucleons bound in the heavier nuclei. This is demonstrated with the dashed curve in fig. 9 which represents the deuteron cross-section folded with the nucleon momentum distribution of Ca. The latter was parameterized as [38]

$$P_{\rm F}(p)dp = k_c \cdot p^2 \cdot \left(e^{-p^2/a} + ce^{-p/b}\right) dp\,, \qquad (8)$$
$$k_c = 4\left(\pi^{1/2}a^{3/2} + 8cb^3\right)^{-1}$$

with $a = 0.42$ fm^2, $b = 0.23$ fm, and $c = 0.04$. The folding was done as discussed in [39]. Here, it was neglected that the deuteron excitation function already incorporates the (much smaller) Fermi smearing effects from the deuteron wave function which in principle would have to be defolded before folding with the Ca distribution.

It is tempting to argue that the shift of the peak in the Δ region by ≈ 20 MeV is related to an in-medium modification of the Δ-resonance due to the Δ-nucleus interaction. Analyses of coherent π^0 photoproduction gave indications of a Δ self-energy corresponding to a similar peak shift, almost independent of the nuclear mass [40,41,33]. However, the interpretation is not so simple. The shape of the low-energy side of the peak reflects the superposition of contributions from coherent and quasifree single-π^0 photoproduction which have different energy dependencies. Furthermore, as discussed below, contributions from multi-body absorption effects of the incident photons are important in the high-energy tail of the Δ. Altogether, position and shape of the Δ peak are influenced by several effects of different nature and not simply connected to the in-medium properties of the Δ.

The data for calcium and lead are compared to the BUU calculations in fig. 10. Since by construction the BUU model accounts only for the incoherent part of photoproduction, the data are also shown after subtraction of the contribution from coherent single-π^0 production taken from [33]. The figure demonstrates the strong absorptive character of the FSI. The calculation without FSI overestimates the lead data almost by a factor of four, but the inclusion of FSI produces a reasonable description of the data. The two models for the P_{33} in-medium widths lead to similar results. The inclusion of the spreading potential gives a larger suppression of the cross-section. The broad structure of the first resonance peak cannot be reproduced by the values used for the P_{33} collision width but an increase much beyond 100 MeV at density ρ_0 would lead to an even stronger suppression of the cross-section and is not

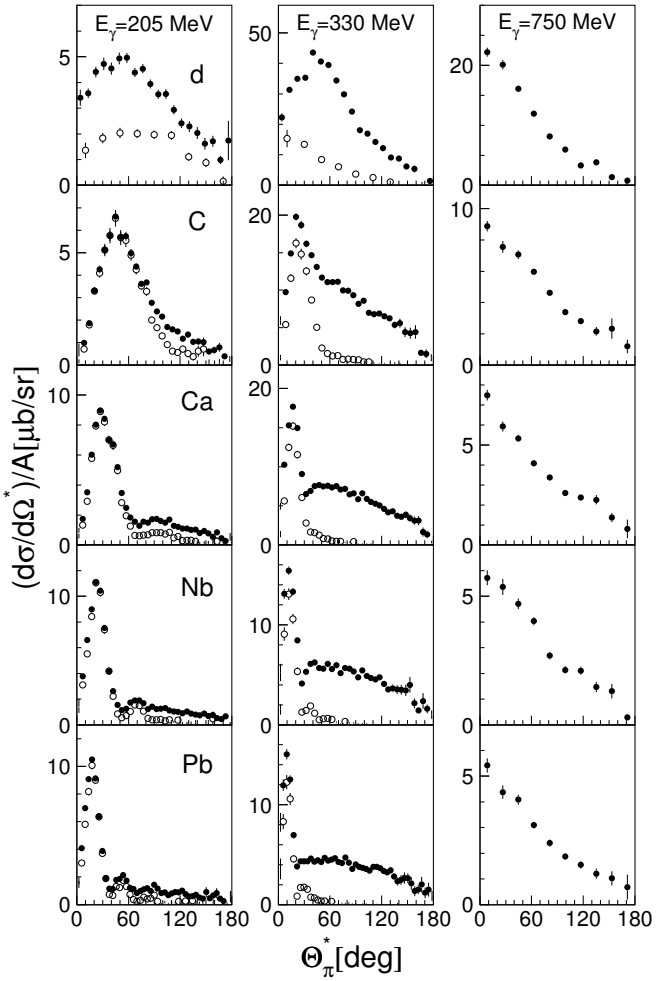

Fig. 11. Angular distributions in the photon-nucleus cm frame scaled by the mass number. Full symbols: inclusive cross-section, this work; open symbols: coherent π^0 production [33].

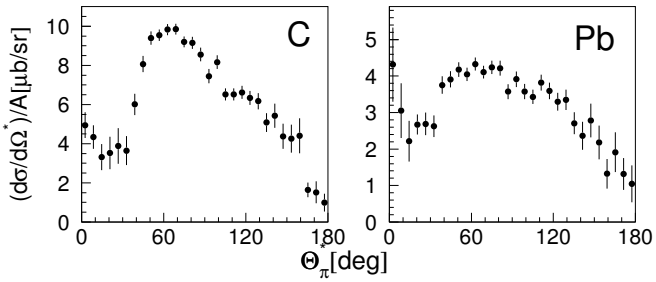

Fig. 12. Angular distributions without coherent π^0 photoproduction in the photon-nucleus cm frame scaled by the mass number for incident-photon energies from 325–335 MeV.

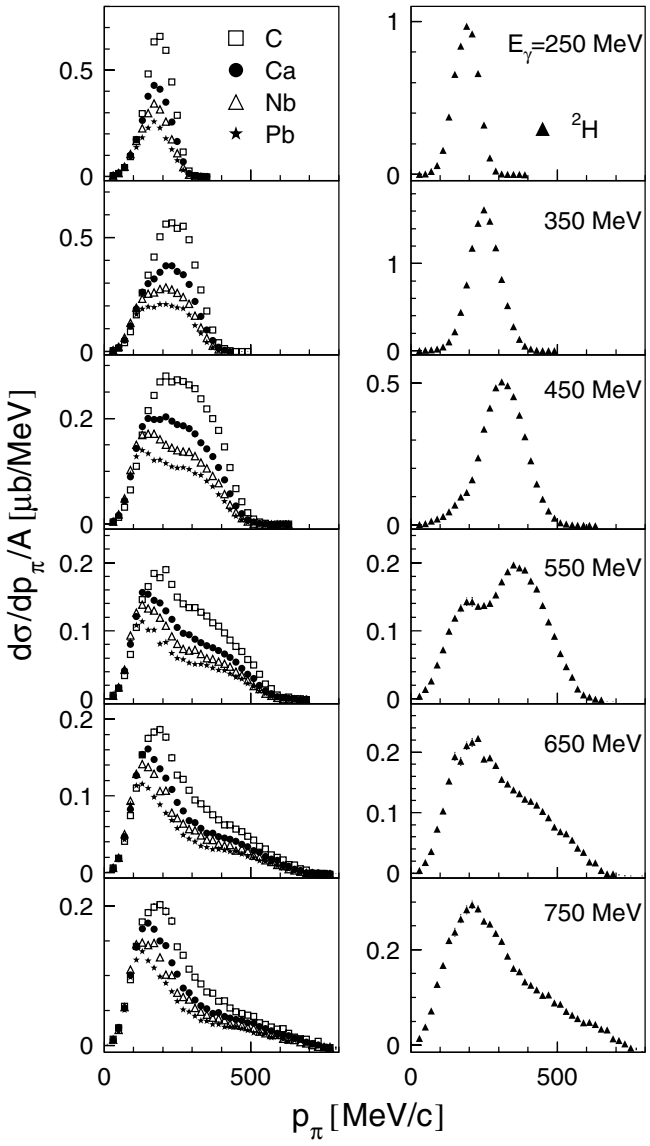

Fig. 13. Distributions of the pion lab momenta for different intervals of incident-photon energy. Left-hand side: heavy nuclei; right-hand side: deuterium.

justified by theoretical models. However, it is known [42] that two-body absorption mechanisms like $\gamma NN \to N\Delta$ are non-negligible in this energy range. Such contributions are not included in the BUU model.

Typical angular distributions are summarized in fig. 11. The contribution from coherent single-π^0 photoproduction is clearly visible for incident-photon energies up to the Δ-resonance region. It disappears at higher photon energies where the distributions are similar for all nuclei. The forward peaking at high photon energies is a consequence of the frame choice (photon-nucleus cm system). Due to the lack of the coherent part, the model calculations cannot reproduce the low-energy angular distributions. Subtraction of the coherent part would not help, since, as discussed for the deuteron in [14,43], the coherent and quasifree parts are somewhat interconnected via nucleon final-state interaction. The effect is also observed for the heavy nuclei. As an example the angular distributions of the quasifree part around incident-photon energies of 330 MeV are shown in fig. 12. The angular distributions are significantly depleted at forward angles where some strength is re-distributed to the coherent part.

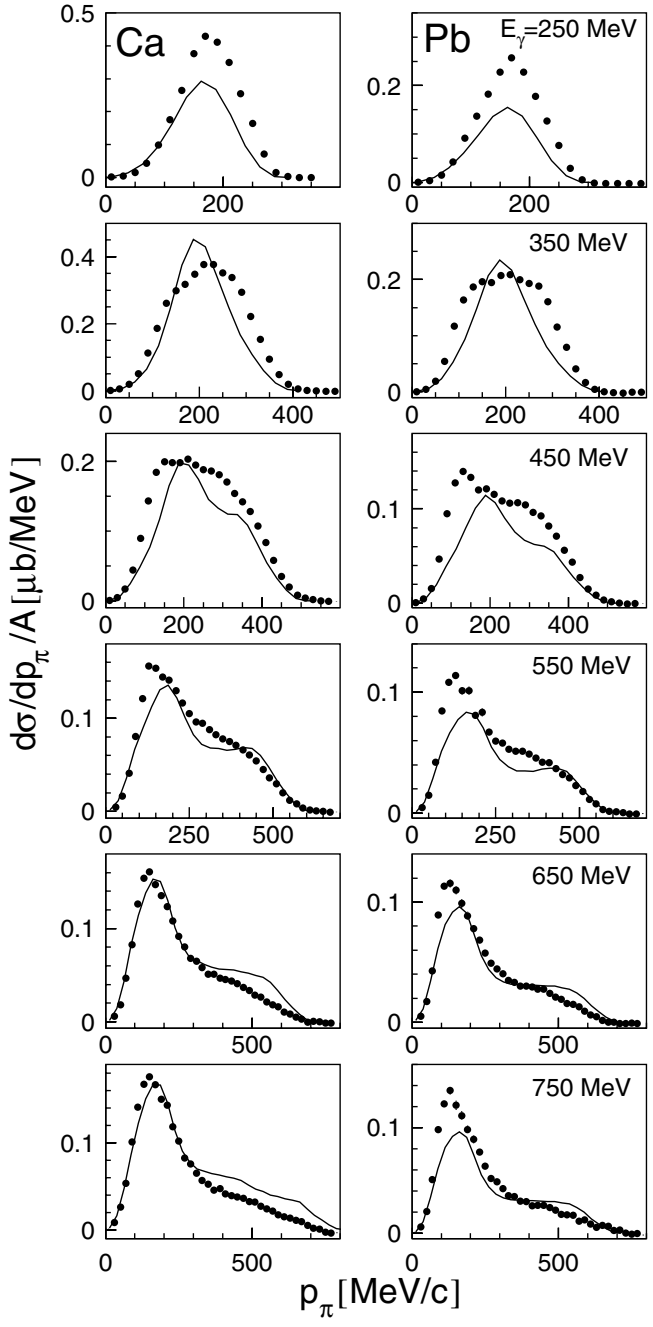

Fig. 14. Distributions of the pion lab momenta for calcium (left-hand side) and lead (right-hand side) compared to BUU calculations. Data and model results are averaged over 100 MeV wide bins of incident-photon energies, the central values are given in the plot. The calculation used the spreading potential of Hirata *et al.*

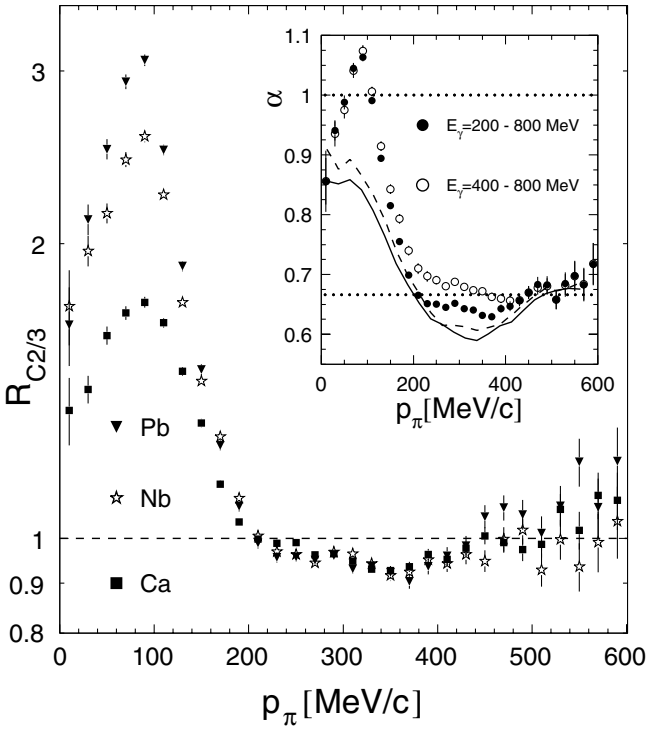

Fig. 15. Scaling of the momentum dependence of the differential cross-section with the nuclear mass number A. The main plot shows the ratio $R_{C2/3}$ (see eq. (9)) for Ca, Nb and Pb. The insert shows the fitted coefficient α (see eq. (10)) averaged over two ranges of incident-photon energy. Curves: BUU results (solid: spreading potential [37], dashed: Oset parameterization [36]). Both averaged over 400–800 MeV photon energy.

The momentum distributions of the pions are summarized in fig. 13. These spectra show the influence of FSI effects. Apart from two-body effects in the absorption of the photons, the distributions from the deuteron can be regarded as source spectra of the pions, which are then modified for the heavier nuclei by FSI. At the lowest incident-photon energies spectra from the deuteron and the heavy nuclei are similar. Up to energies of 500 MeV, the distributions measured on the deuteron simply shift to larger momenta corresponding to the quasifree kinematics of single-π^0 production. However, the nuclei in this energy region show already a re-distribution of the pion momenta to smaller values. At small momenta the nuclear data scale with the mass number A which indicates a large mean free path of the pions in this range. At even higher incident-photon energies the pion spectra from the deuteron develop a double bump structure. The additional peak at lower momenta comes from double-pion production reactions. At the highest energies this contribution becomes dominant. The contribution from single-pion production for the heavier targets is suppressed due to FSI effects even at lower incident-photon energies. The data for calcium and lead are compared to the BUU results obtained with the spreading potential [37] in fig. 14. The discrepancy at the lowest incident-photon energies is mainly due to coherent π^0 photoproduction which contributes to the data but is not included in the BUU calculations. The general trend of the FSI effects, *i.e.* the shift of strength to small pion momenta, is reproduced by the model.

The FSI effects are closely related to the absorption properties of nuclear matter for pions, that is the mean free path of pions in nuclear matter. The momentum dependence of this effect is analyzed in fig. 15. The main plot

shows the ratio of the cross-sections from the three heaviest nuclei with respect to carbon, normalized to $A^{2/3}$. It is defined via

$$R_{C2/3} = \frac{\sigma(A)/A^{2/3}}{\sigma(^{12}\mathrm{C})/12^{2/3}} \ . \tag{9}$$

The insert shows the scaling exponent α obtained from fits of the mass dependence of the data with the ansatz:

$$\sigma(A) \propto A^{\alpha} \ . \tag{10}$$

The differential cross-sections are averaged over the entire range of incident-photon energies 200–800 MeV. The scaling coefficient is also shown for incident-photon energies above 400 MeV, where contributions from coherent π^0 photoproduction are negligible. Coherent contributions could obscure the scaling, since their production (before FSI) is not simply proportional to the mass number A. However, the plot shows that their influence is small. Both figures demonstrate qualitatively the same behavior. For pion momenta larger than roughly 200 MeV/c, the cross-sections scale like $A^{2/3}$, which indicates strong absorption and small mean free paths of the pions. At smaller pion momenta the nuclei become more transparent for pions and the cross-sections scale with the volume. This is expected since pions with a momentum of 227 MeV/c can excite a nucleon to the nominal mass of the Δ. Therefore, at momenta larger than $\approx$ 200 MeV/c pions are very likely re-absorbed via $\pi N \to \Delta$. This explains also qualitatively the shift of strength to small pion momenta in fig. 13. Only those pions which are produced with small momenta or acquire small momenta after absorption and re-emission processes are likely to escape from the nucleus. Contributions from larger pion momenta stem mainly from the nuclear surface region. These momentum distributions are therefore very sensitive to the FSI effects and thus a valuable testing ground for model predictions. The BUU calculations show qualitatively similar behavior, however they do not reproduce the strong peak at pion momenta around 100 MeV/c. This could indicate that the mean free path for low pion momentum is underestimated. However, one should be aware that the coefficient α does not only depend on the mean free path of the pions. It can be also influenced to some extent by the re-distribution of the pion momenta due to the absorption and re-emission processes.

We have already noted in the discussion of the total inclusive cross-section that in case of the heavier nuclei the valley between the first and second resonance region is much shallower than for the deuteron. This could be due either to FSI effects or to the initial photo-pion production mechanism. The two possibilities can be tested by a comparison of the momentum spectra to the deuteron data. For this purpose the ratio

$$R_d = \frac{\sigma(A)/A^{2/3}}{\sigma(^2\mathrm{H})/2} \ , \tag{11}$$

which compares the nuclear data to the average nucleon cross-section is plotted in fig. 16 as a function of the pion momenta for different regions of incident photon energies. At a given pion momentum the absorption probability should be independent of the incident-photon energy. For the lowest incident-photon energies the ratio shows the expected behavior which reflects the momentum dependence of the pion mean free path discussed above: It is large for small pion momenta and then drops to unity around $p_\pi \approx 200$ MeV/c. However, at incident-photon energies between 500 and 600 MeV, the ratio is always larger than unity, in particular for momenta in the range between 200 and 350 MeV/c. This is an indication that for the heavy nuclei in the intermediate energy range a certain fraction of pions is indeed produced via mechanisms which do not operate or are less important for the deuteron. Possible candidates are contributions from multi-body absorption mechanisms like $\gamma NN \to N\Delta$ (see, *e.g.*, [42]), in-medium effects of any of the involved partial reaction channels, or charge exchange reactions which effectively transfer strengths from final states like $\pi^+\pi^-$ to the inclusive π^0 channel. However, the latter are a less likely cause since the BUU calculations do not reproduce the additional strength at intermediate photon energies although they include the charge exchange reactions.

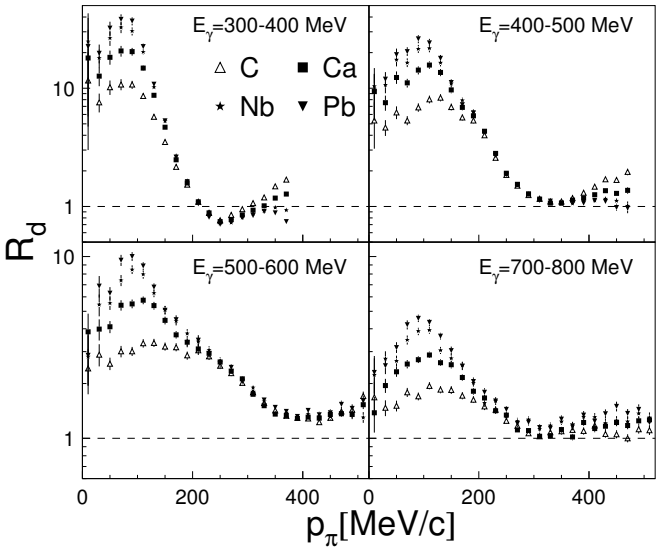

Fig. 16. Ratio of cross-section from heavy nuclei and deuterium. The ratio R_d (see eq. (11)) for carbon, calcium, niobium and lead is plotted.

5.2 Semi-exclusive reaction channels

In the following we will decompose the inclusive cross-section into partial reaction channels. The photoproduction of η-mesons contributes to the inclusive π^0 cross-section via the $\eta \to 3\pi^0$ and $\eta \to \pi^0\pi^+\pi^-$ decays. Since the η is long lived, it always decays outside the nuclei, so that these pions do not undergo FSI effects. The contribution to pion production is obtained directly from the measured 2γ decay channel of the η-mesons and the respective branching ratios. The scaled total cross-section σ_η for η photoproduction from nuclei are compared in fig. 17

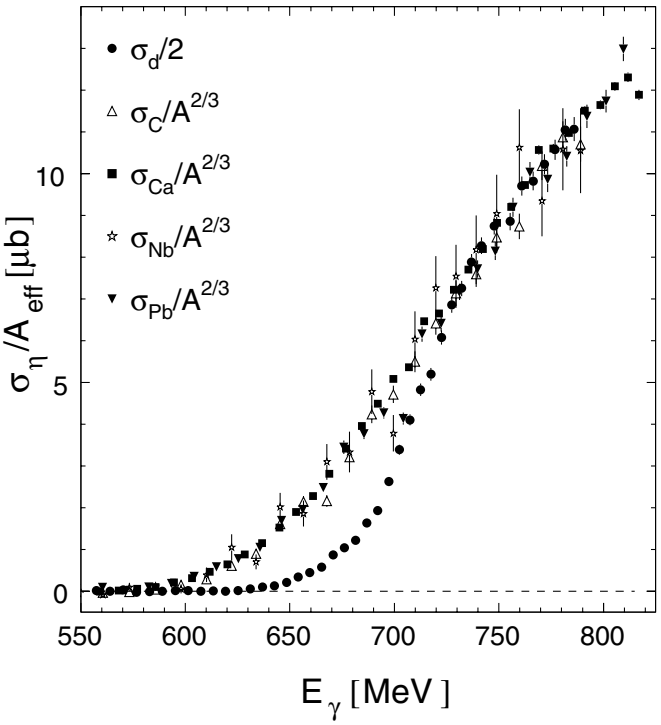

Fig. 17. Total cross-section σ_η of η photoproduction from heavy nuclei. The data for carbon and niobium are taken from [18], the data for calcium and lead are from the present analysis of the measurements with the improved setup. The nuclear cross-sections are normalized to $A^{2/3}$ and compared to the average cross-section from the nucleon ($\sigma_d/2$) [39].

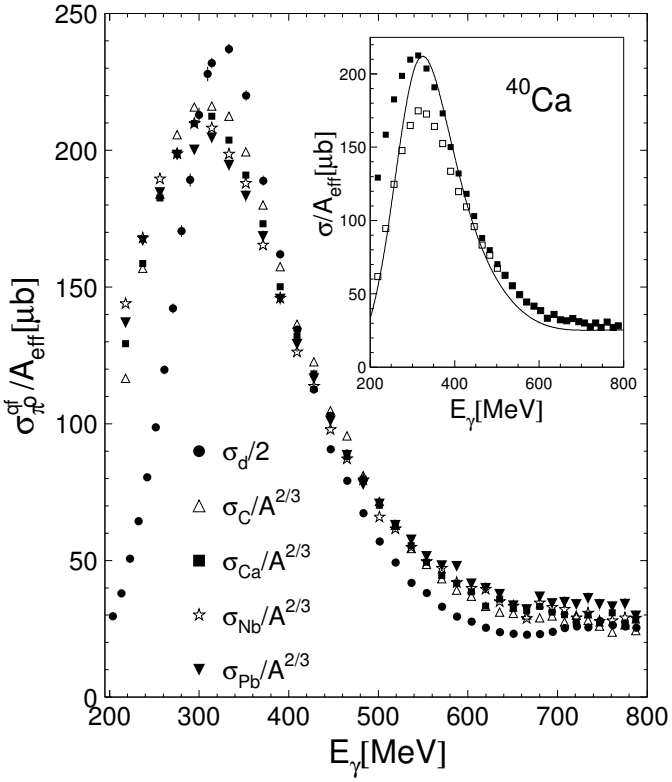

Fig. 18. Total cross-section $\sigma^{\rm qf}_{\pi^0}$ of single quasifree π^0 photoproduction from heavy nuclei. The nuclear cross-sections are normalized to $A^{2/3}$ and compared to the average cross-section from the nucleon ($\sigma_d/2$). The insert compares for ^{40}Ca $\sigma^{\rm qf}_{\pi^0}$ (full points) to the cross-section with subtracted coherent part. The curve corresponds to the deuteron cross-section ($\sigma_d/2$) folded with the momentum distribution of nucleons in calcium.

to the deuteron data [39]. In case of carbon and niobium, previous data from [18] are used. For calcium and lead results with much improved statistical quality, obtained with the improved setup, are shown. The nuclear data follow an $A^{2/3}$ scaling and agree above the production threshold on the free nucleon ($E_{\rm thr} = 706$ MeV) with the average nucleon cross-section. In the immediate threshold region the reaction is only possible for large momenta of the bound nucleons anti-parallel to the incident-photon momentum. The reaction on the deuteron is therefore suppressed in the threshold region since the Fermi momenta are much smaller than for the heavier nuclei.

Quasifree single-π^0 photoproduction was extracted with the kinematical cuts discussed in sect. 3.2. Results for the second resonance region were already published in [24]. Again the nuclear cross-sections $\sigma^{\rm qf}_{\pi^0}$ scale like $A^{2/3}$ (see fig. 18) and are similar to the average nucleon cross-section. The difference between the scaled nuclear and deuteron cross-sections at low incident-photon energies is related to coherent π^0 photoproduction which is more important for the heavier nuclei. Note that in this channel in contrast to the inclusive reaction the position of the Δ peak is shifted to a lower incident-photon energy for the heavier nuclei.

In fig. 19, the data for calcium and lead are compared to the results of the BUU model. Again, the data are also plotted after subtraction of contributions from coherent π^0 production to facilitate a better comparison with the model. The calculations include the same missing-energy cuts as the experiment. The curves show a similar behavior as in the case of the inclusive cross-section in fig. 10. In particular, the discrepancy at intermediate photon energies also shows up here. This suggests that two-body photon absorption mechanisms also contribute to this channel. In the second resonance region, the calculations overestimate the data. However, this does not necessarily mean that this is solely due to an overestimate of the D_{13} contribution which in the calculations only amounts to roughly 25% of the total cross-section for $E_\gamma = 700$ MeV.

The experimental results for double-π^0 photoproduction are summarized in fig. 20 ($\sigma_{2\pi^0}$). In the first measurement, the limited solid angle did not allow an analysis of events with four photons. Those data are therefore limited to the practically background-free energy range below the η-production threshold (triangles in the figure for C, Ca, Nb, Pb). The measurement with the improved setup allowed the clean extraction of the cross-section from 4-photon events via a missing-mass analysis. Background from η decays was subtracted. The results for calcium and lead (filled circles) are shown in the figure up to a maximum photon energy of 800 MeV. All nuclear data scale

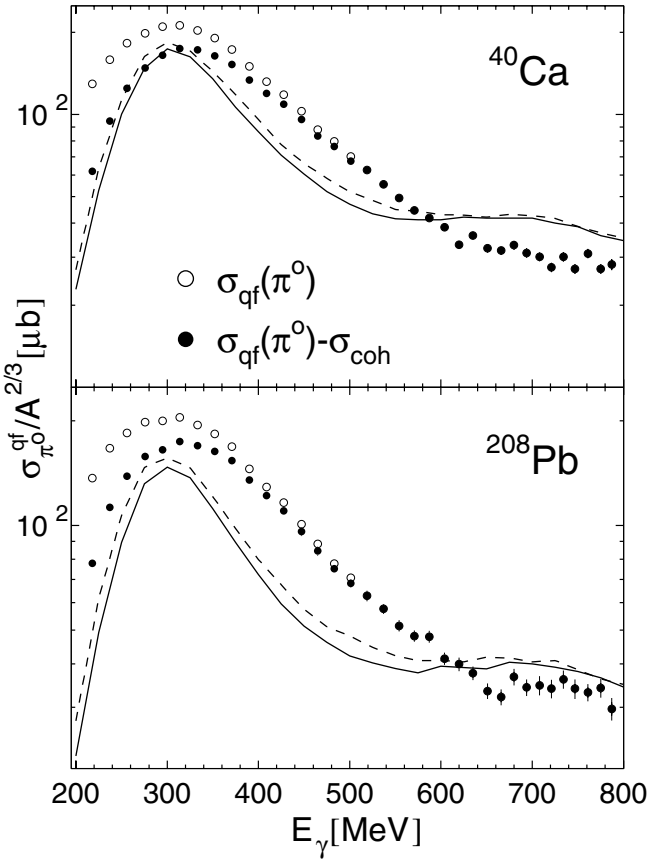

Fig. 19. Comparison of the single-π^0 cross-section to BUU model calculations for calcium and lead. Open symbols: single-π^0 production, filled symbols: coherent part subtracted. Curves: BUU, Δ in-medium width from Oset parameterization (dashed line) [36] or Hirata (solid line) [37].

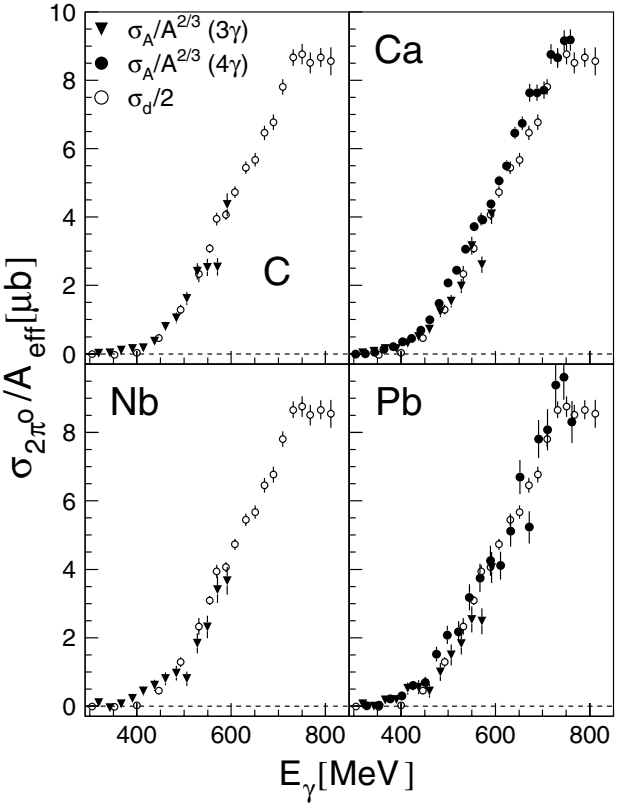

Fig. 20. Total cross-section $\sigma_{2\pi^0}$ of double-π^0 photoproduction normalized to $A^{2/3}$ and compared to the average nucleon cross-section ($\sigma_d/2$).

like $A^{2/3}$ and agree with the average nucleon cross-section $\sigma_d/2$ taken from [34].

The same result is found for $\pi^0\pi^\pm$ production which is shown in fig. 21. The data for calcium and lead again scale like $A^{2/3}$. Also shown in this figure are the cross-sections for $\gamma p \to n\pi^0\pi^+$ [44] and $\gamma n \to p\pi^0\pi^-$ [45]. Finally, the cross-section for $\gamma d \to np\pi^0\pi^\pm$ was obtained from the inclusive π^0 photoproduction cross-section $\sigma_{\rm incl}$ on the deuteron by subtraction of the cross-sections from all other partial channels (see eq. (1)). It is obvious from the figure that also in this case the nuclear cross-sections scaled by $A^{2/3}$ agree with the average nucleon cross-section.

The results for the semi-exclusive quasifree reaction channels thus can be summarized in the following way: all investigated nuclear cross-sections are related to a good approximation to the deuteron cross-section by

$$\frac{\sigma_x^{\rm qf}(A)}{A^{2/3}} \approx \frac{\sigma_x^{\rm qf}(d)}{2} \ . \qquad (12)$$

The scaling among the heavier nuclei holds even when the comparison to the deuteron is disturbed, *e.g.* by the effects of coherent single-π^0 production at low photon energies

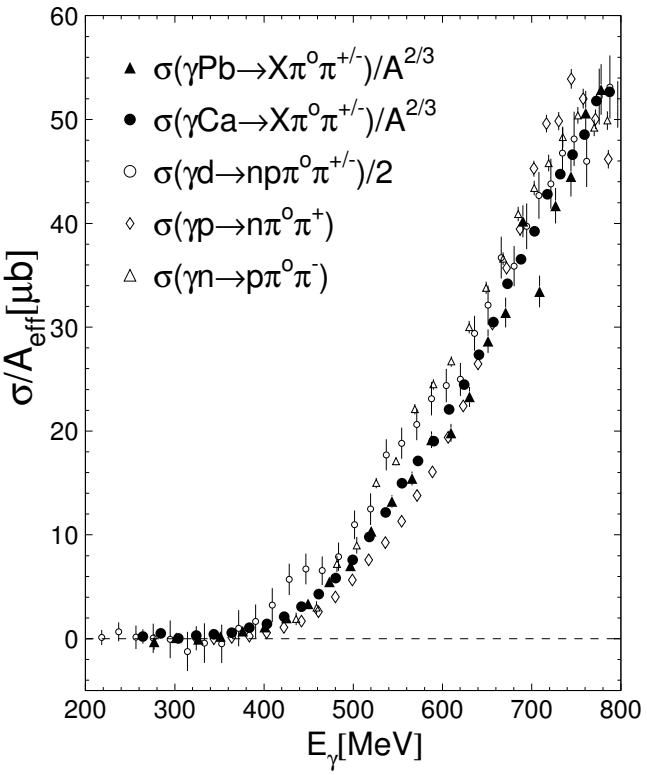

Fig. 21. Total cross-section of $\pi^0\pi^\pm$ photoproduction normalized to $A^{2/3}$ and compared to the free nucleon cross-section (see text).

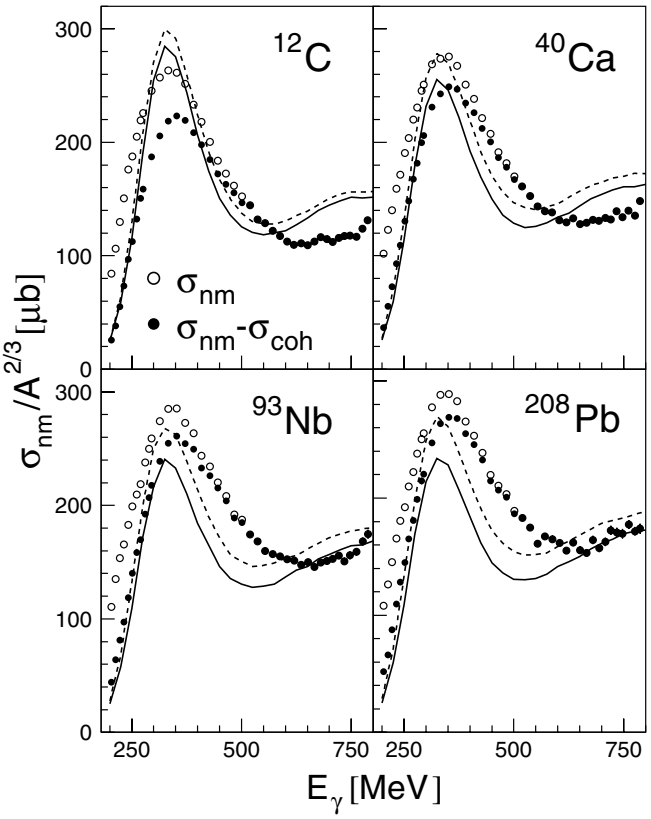

Fig. 22. Comparison of the total cross-section for neutral meson production ($\sigma_{\rm nm}$, see eq. (2)) to BUU model calculations. Open symbols: $\sigma_{\rm nm}$, filled symbols: coherent single-π^0 production subtracted. Curves: BUU, Δ in-medium width from Oset parameterization (dashed line) [36] or Hirata (solid line) [37].

and or by effects of Fermi smearing close to the η threshold. The $A^{2/3}$ scaling is the limiting case of strong FSI effects due to the short pion mean free path. This means that the quasifree exclusive reactions probe only the nuclear surface region. Since the properly scaled nuclear cross-sections agree with the deuteron cross-section no significant in-medium effects are observed for the low-density surface zone of the nuclei.

With the knowledge of the nuclear cross-sections for η and double-π^0 photoproduction, it is possible to correct the contribution from higher pion multiplicity channels to the total inclusive cross-section and thus to determine the part of the total photoabsorption cross-section ($\sigma_{\rm nm}$, see eq. (2)) which corresponds to events with at least one π^0 or one η in the final state. The result is compared in fig. 22 to the BUU model calculations. Again also the results with subtracted coherent part are shown. The calculations show essentially the same behavior as already observed for the inclusive cross-section in fig. 9. In particular, for the lighter nuclei the second resonance peak is still overestimated and the valley between the Δ-resonance and the second resonance region is too pronounced. In the case of carbon it should be noted that the assumptions of the BUU model are much less fulfilled for such a light nucleus with a relatively large surface/volume ratio. However, a further observation is that while for the heaviest nuclei the agreement in the second resonance region is much improved, the disagreement in the "valley region" around 500 MeV grows. This could mean that the agreement in the second resonance region is only accidental because the contributions from two-body absorption effects are neglected. A quantitative investigation of the influence of the two-body absorption effects, in particular the dependence on the incident-photon energy, is therefore highly desirable.

6 Summary and conclusion

Cross-section data for meson photoproduction from nuclei in the energy range from 200–800 MeV have been obtained for all final states which involve at least one neutral meson. The inclusive data have been used for an analysis of the pion final-state interaction in nuclei. The momentum-dependent absorption properties of nuclear matter show qualitatively the expected behavior: strong absorption for pions which can excite the Δ-resonance on the nucleon and almost perfect transparency of the nuclei for low-energy pions. The absorption properties within the BUU model show a similar behavior, although no quantitative agreement is achieved for small pion momenta.

The cross-sections of all exclusive quasifree meson production reactions scale with the nuclear surface ($A^{2/3}$) and agree to a good approximation with the respective cross-sections for the deuteron normalized to the deuteron mass number. This means that no significant in-medium effects are observed for the quasifree processes which test the low-density surface region of the nuclei. Even the inclusive data, which include some fraction of non-quasifree reactions, show a clear signal for the second resonance bump. This is an indication that the complete suppression of this bump observed in total photoabsorption reactions is not the result of trivial nuclear effects like Fermi motion. The observation that the excitation function for meson production from the surface region of nuclei has a different energy dependence than total photoabsorption in the nuclear volume seems to indicate density-dependent in-medium effects.

The experimental data have been compared in detail to calculations in the framework of the BUU model. It is observed that the model is remarkably successful in reproducing FSI effects such as pion absorption and the shift of strength in the pion momentum spectra. However, some discrepancies on the quantitative level remain. In the Δ-resonance region the inclusion of realistic P_{33} in-medium widths lead to a better description of the data. Also in the second resonance region the calculations are close to the data although especially for lighter nuclei an overestimation is visible. The intermediate energy region is not reproduced which is in line with the theoretical findings in photoabsorption that multi-body photon absorption mechanisms, which are not included in the BUU model, play an important role in this region. Effenberger *et al.* [46] have calculated such effects for photoabsorption on ^{40}Ca. They find them negligible below incident-photon

energies of 300 MeV and rising to a 25% effect at photon energies around 500 MeV. A comparable contribution to pion production would much improve the agreement between data and calculations in this energy region. However, at present it is not known how much the two-body effects will contribute at higher incident-photon energies. A quantitative treatment of these effects is thus necessary in future theoretical studies of the in-medium effects in the second resonance region.

We wish to acknowledge the excellent support of the accelerator group of MAMI, as well as many other scientists and technicians of the Institut für Kernphysik at the University of Mainz. We thank M. Röbig-Landau for his contribution to the calibration and analysis of the inclusive data. J. Lehr would like to thank M. Post for many valuable discussions. This work was supported by Schweizerischer Nationalfonds, Deutsche Forschungsgemeinschaft, and the UK Engineering and Physical Sciences Research Council.

References

1. W. Peters *et al.*, Nucl. Phys. A **632**, 109 (1998).
2. C.L. Korpa, M.F.M. Lutz, Nucl. Phys. A **742**, 305 (2004).
3. M. Post, S. Leupold, U. Mosel, Nucl. Phys. A **741**, 81 (2004).
4. G.E. Brown, M. Rho, Phys. Rev. Lett. **66**, 2720 (1991).
5. R. Rapp, J. Wambach, Adv. Nucl. Phys. **25**, 1 (2000).
6. Th. Frommhold *et al.*, Z. Phys. A **350**, 249 (1994).
7. N. Bianchi *et al.*, Pys. Lett. B **325**, 333 (1994).
8. B. Krusche, S. Schadmand, Prog. Part. Nucl. Phys., **51**, 399 (2003).
9. K. Büchler *et al.*, Nucl. Phys. A **570**, 580 (1994).
10. A. Braghieri *et al.*, Phys. Lett. B **363**, 46 (1995).
11. B. Krusche *et al.*, Phys. Rev. Lett. **74**, 3736 (1995).
12. M. MacCormick *et al.*, Phys. Rev. C **53**, 41 (1996).
13. F. Härter *et al.*, Phys. Lett. B **401**, 229 (1997).
14. B. Krusche *et al.*, Eur. Phys. J. A **6**, 309 (1999).
15. J.A. Gomez Tejedor, E. Oset, Nucl. Phys. A **600**, 413 (1996).
16. M. Hirata, K. Ochi, T. Takaki, Phys. Rev. Lett. **80**, 5068 (1998).
17. B. Krusche *et al.*, Phys. Lett. B **397**, 171 (1997).
18. M. Röbig-Landau *et al.*, Phys. Lett. B **373**, 45 (1996).
19. T. Inoue, E. Oset, Nucl. Phys. A **710**, 354 (2002).
20. M. Effenberger, A. Hombach, S. Teis, U. Mosel, Nucl. Phys. A **614**, 501 (1997).
21. R.C. Carrasco, Phys. Rev. C **48**, 2333 (1993).
22. T. Yorita *et al.*, Phys. Lett. B **476**, 226 (2000).
23. J. Lehr, M. Post, U. Mosel, Phys. Rev. C **68**, 044601 (2003).
24. B. Krusche *et al.*, Phys. Rev. Lett. **86**, 4764 (2001).
25. J. Lehr, U. Mosel, Phys. Rev. C **64**, 042202 (2001).
26. M. Effenberger, E.L. Bratkovskaya, U. Mosel, Phys. Rev. C **60**, 044614 (1999).
27. J. Lehr, M. Effenberger, U. Mosel, Nucl. Phys. A **671**, 503 (2000).
28. I. Anthony *et al.*, Nucl. Instrum. Methods A **301**, 230 (1991).
29. Th. Walcher, Prog. Part. Nucl. Phys. **24**, 189 (1990).
30. R. Novotny, IEEE Trans. Nucl. Sci. **38**, 379 (1991).
31. A.R. Gabler *et al.*, Nucl. Instrum. Methods A **346**, 168 (1994).
32. R. Brun *et al.*, GEANT, Cern/DD/ee/84-1, 1986.
33. B. Krusche *et al.*, Phys. Lett. B **526**, 287 (2002).
34. V. Kleber *et al.*, Eur. Phys. J. A **9**, 1 (2000).
35. M. Wolf *et al.*, Eur. Phys. J. A **9**, 5 (2000).
36. E. Oset, L.L. Salcedo, Nucl. Phys. A **468**, 631 (1987).
37. M. Hirata, J.H. Koch, F. Lenz, E.J. Moniz, Ann. Phys. (N.Y.) **120**, 205 (1979).
38. W. Cassing *et al.*, Z. Phys. A **349**, 77 (1994); W. Cassing, private communication.
39. B. Krusche *et al.*, Phys. Lett. B **358**, 40 (1995).
40. F. Rambo *et al.*, Nucl. Phys. A **660**, 69 (1999).
41. D. Drechsel *et al.*, Nucl. Phys. A **660**, 423 (1999).
42. R.C. Carrasco, E. Oset, Nucl. Phys. A **536**, 445 (1992).
43. U. Siodlaczek *et al.*, Eur. Phys. J. A **10**, 365 (2001).
44. W. Langgärtner *et al.*, Phys. Rev. Lett. **87**, 052001 (2001).
45. A. Zabrodin *et al.*, Phys. Rev. C **55**, R1617 (1997).
46. M. Effenberger, A. Hombach, S. Teis, U. Mosel, Nucl. Phys. A **613**, 353 (1997).